metals

MDPI

Article

In-Situ Alloying of CoCrFeNiX High Entropy Alloys by Selective Laser Melting

Lucy Farquhar *, George Maddison, Liam Hardwick, Frances Livera, Iain Todd and Russell Goodall

Department of Materials Science and Engineering, University of Sheffield, Sheffield S1 3JD, UK; gmaddison1@sheffield.ac.uk (G.M.); liam.hardwick@sheffield.ac.uk (L.H.); fslivera1@sheffield.ac.uk (F.L.); iain.todd@sheffield.ac.uk (I.T.); r.goodall@sheffield.ac.uk (R.G.)

* Correspondence: laufarquhar1@sheffield.ac.uk

Abstract: High Entropy Alloys are a class of alloys which have been shown to largely exhibit stable microstructures, as well as frequently good mechanical properties, particularly when manufactured by additive manufacturing. Due to the large number of potential compositions that their multi-component nature introduces, high throughput alloy development methods are desirable to speed up the investigation of novel alloys. Here, we explore once such method, in-situ alloying during Additive Manufacture, where a powder of a certain pre-alloyed composition is mixed with the required composition of powder of an additional element, such that alloying takes place when powders are melted during the process. To test the effectiveness and capability of the approach, selective laser melting has been used to manufacture pre-alloyed CoCrFeNi, and also CoCrFeNiCu and CoCrFeNiTi alloys by combining pre-alloyed CoCrFeNi powder with elemental powders of Cu and Ti. Processing parameter variations are used to find the highest relative density for each alloy, and samples were then characterised for microstructure and phase composition. The CoCrFeNi alloy shows a single phase face centred cubic (FCC) microstructure, as found with other processing methods. The CoCrFeNiCu alloy has a two phase FCC microstructure with clear partitioning of the Cu, while the CoCrFeNiTi alloy has an FCC matrix phase with NiTi intermetallics and a hexagonal close packed (HCP) phase, as well as unmelted Ti particles. The microstructures therefore differ from those observed in the same alloys manufactured by other methods, mainly due to the presence of areas with higher concentrations than usually encountered of Cu and Ti respectively. Successful in-situ alloying in this process seems to be improved by the added elemental powder having a lower melting point than the base alloy, as well as a low inherent tendency to segregate. While not producing directly comparable microstructures however, the approach does seem to offer advantages for the rapid screening of alloys for AM processability, identifying, for example, extensive solid-state cracking in the CoCrFeNiTi alloy.

Keywords: high entropy alloys; additive manufacturing; selective laser melting; laser processing; in-situ alloying; microstructure

Citation: Farquhar, L.; Maddison, G.; Hardwick, L.; Livera, F.; Todd, I.; Goodall, R. In-Situ Alloying of CoCrFeNiX High Entropy Alloys by Selective Laser Melting. *Metals* **2022**, *12*, 456. https://doi.org/10.3390/met12030456

Academic Editor: Babak Shalchi Amirkhiz

Received: 28 January 2022
Accepted: 4 March 2022
Published: 8 March 2022

1. Introduction

High Entropy Alloys (HEAs) are a novel group of alloys which have attracted attention in recent years due to their microstructural stability and mechanical properties. HEAs were originally defined as alloys with 5–13 elements with concentrations varying between 5–35 at%, however that definition has since been expanded to include an even broader range of alloys, including those with 4 elements [1–4]. Since HEAs contain multiple elements with similar composition the expectation is that the microstructure will be complex with multiple phases; however in reality many have a stable single phase, in part due their high entropy. An example of this is the first reported HEA, discovered by Cantor et al., which contained the elements CoCrFeNiMn in equiatomic proportions, and resulted in a stable

single phase microstructure [5]. This alloy has provided a basis for much of the further research into HEAs of this type, including into processing by additive manufacturing (AM).

AM is a process where parts are built up layer by layer to often create complex geometries and internal features which cannot be achieved by other manufacturing methods. Often AM parts are also exposed to high cooling rates which can result in microstructural refinement as well as inhibit segregation. One of the most widespread AM methods is selective laser melting (SLM) and therefore this method was selected for use in this work. HEAs in general have been extensively researched for use in AM, as compiled in some recent review articles [6,7]. However, early work on CoCrFeNi alloys specifically, for AM mainly focused on laser cladding, including where CoCrFeNiCu was shown to have excellent corrosion resistance [8–10]. This contrasts with other work on the corrosion of CoCrFeNiCu in a bulk as-cast form, which indicates that the corrosion resistance is lower than typical stainless steels [11]. There are also examples of this type of HEA also being produced by Direct Laser Deposition (DLD), where Xiang et al. noted that there was significant solute-trapping resulting in a more homogeneous microstructure compared to cast specimens of the CoCrFeNiMn alloy [12–14].

Previously, in-situ alloying has been used to manufacture HEAs with varying success and without comparison between elements. The CoCrFeMnNi alloy was manufactured via SLM by alloying the Mn in-situ, and this resulted in the vaporisation of some of the Mn, and a reduction of Mn in some areas [15]. Cagirici et al. also recently added Ti to the pre-alloyed CoCrFeMnNi and used Scanning Electron Beam Melting (SEBM) for in-situ alloying, resulting in a homogeneous distribution of Ti, as well as the appearance of surface cracks and brittle phases as the Ti concentration was increased [16]. In-situ alloying of elemental powders alone has also been used to manufacture refractory HEAs with some vaporisation of the lower melting point elements [17–20]. As well as also being utilised to manufacture refractory HEAs using sintering, resulting in parts with high but uneven density, due to differing spreading abilities of the elements [21].

This work focuses primarily on in-situ alloying of Cu and Ti elemental additions to pre-alloyed CoCrFeNi powder using the SLM process to produce equiatomic HEAs. The reason for completing this research is to try and assess the validity of mixing additional elemental powders to a base powder to manufacture a fully alloyed sample with a homogeneous microstructure. In this work, the term in-situ refers only to the melting and alloying of multiple powders together using the SLM process. It aims to discover what considerations are necessary and to ascertain whether this technique is valid to accelerate further alloy development, as it avoids the need to manufacture each individual alloy in quantity and in powder form for experimental AM trials. The SLM of the CoCrFeNi alloy itself without any additions has been researched previously and has shown a single phase face-centred cubic (FCC) microstructure [2,22]. Multiple different investigations into CoCrFeMnNi have been completed, also showing a single phase FCC microstructure [15,23–29]. The CoCrFeNiAl system made via SLM has also a proved a popular alloy due to its tendency to form a dual phase FCC and body centred cubic (BCC) structure with a high hardness and corrosion resistance [30–33]. Slight variations on this type of alloy with AlCrCuFeNi [34], AlCoCrCuFeNi [35] and AlCoCuFeNi [36] were also manufactured, all with a high crack susceptibility.

Cu and Ti were selected for this research as they show markedly different behaviour and microstructural consequences when alloyed with CoCrFeNi. They also have melting points above (1688 °C for Ti) and below (1084 °C for Cu) that of the CoCrFeNi alloy which is 1414 °C [2], therefore providing insight into the importance of relative melting temperature for in-situ alloying. Focussing on the alloys concerned in this study, CoCrFeNiTi-type alloys have been manufactured via SLM by Fujieda et al. where $Co_{1.5}CrFeNi_{1.5}Ti_{0.5}Mo_{0.1}$ shows an impressive tensile strength of 1178.0 MPa and elongation of 25.8% [37–39]. A $CoCrFeNiTi_{0.2}$ alloy has also been made by laser cladding which showed a eutectic lamellar microstructure of an FCC and a Laves phase [40]. Shun et al. also previously made CoCrFeNiTi-type alloys by arc-melting, showing the appearance of a plate like structure

containing a R phase and a Laves phase as the concentration of Ti was increased [41]. The CoCrFeNiCu alloy has not been reported to have been manufactured by SLM, however it has been made by laser cladding with small additions of Mo, Mn and Si, and showed a single phase FCC microstructure [8]. When manufactured by other methods (primarily arc-melting), this alloy consistently has a dual phase FCC microstructure with Cu-lean grains surrounded by a Cu-enriched FCC phase on the grain boundaries [42–46].

2. Materials and Methods

Each SLM build used gas atomised, pre-alloyed, nominally equimolar CoCrFeNi powder, the measured composition of which, before the process, is shown in Table 1. Elemental powders of Cu and Ti were obtained for combination with this, and were added such that each element had a concentration of 20 at%. All specimens were manufactured using an AconityMINI SLM machine with a maximum laser power of 200 W and a spot size of 70 µm. For the CoCrFeNi samples, 5 mm × 5 mm × 10 mm specimens were produced. For the CoCrFeNiCu 7 mm diameter × 10 mm cylinders were made and for the CoCrFeNiTi 7 mm × 7 mm × 10 mm specimens were produced. Prior to mixing, the particle size for each powder was measured using a laser diffraction particle size analyser (Mastersizer 2000, Malvern, UK). The pre-alloyed CoCrFeNi powder and elemental powders were mixed by tumbling them together on multiple axes for 15 min.

Table 1. Chemical composition of CoCrFeNi powder, analysed using XRF (AMG Superalloys UK) taken from work by Brif et al. using the same powder [2].

Element	Fe	Co	Cr	Ni	Al	Si	Zr	Other
wt.%	23.48	26.28	21.07	27.16	0.14	0.10	0.11	<0.05

Processing parameters have a large effect on material microstructure and properties in SLM, as the melt penetration depth of the laser influences the fusion between layers of the deposited powder. The previous study on SLM of CoCrFeNi by Brif et al. was completed using the Renishaw SLM125 with a pulsed laser system [2]. The AconityMINI uses a continuous laser, meaning the parameters used by Brif et al. could not be directly employed. Therefore, a statistical 'Design of Experiment' (DOE) for each alloy was created using Minitab software by varying the laser power (70–190 W), scanning velocity (400–1300 mm/s) and hatch spacing (20–130 µm) while keeping a constant layer thickness of 30 µm. The power is limited by the maximum power of the AconityMINI which is 200 W, the layer thickness was kept the same for all parts to allow each part to be built on the same build plate in the same run of the machine. Initial microstructural studies were completed using a Clemex optical microscope. The specimens were analysed as-deposited without any subsequent treatment. All specimens were sectioned perpendicular to the layer deposition direction and were prepared by standard grinding and polishing methods. This included polishing with diamond suspension down to 1 µm and finishing with colloidal silica solution with a particle size of 0.05 µm. The relative density of each specimen was calculated by quantifying the internal porosity. This was done by analysing a cross-section and then employing an automatic thresholding procedure in the image analysis software ImageJ [47].

Subsequent phase characterisation was carried out by X-ray Diffraction (XRD) using a Bruker D2 Phaser Diffractomer with a Cu K_α radiation source ($\lambda = 1.54$ Å). Further microstructural characterisation as well as imaging of the powders, was carried out using a FEI Inspect F50 Scanning Electron Microscope (SEM) and Energy Dispersive X-ray Spectroscopy (EDS). The spot size and accelerating voltage were 4 and 20 kV respectively, and the working distance was approximately 10 mm. The software used for EDS analysis was AZtec (Oxford instruments, Oxon, UK).

3. Results

3.1. Powder Analysis

The SEM of images of each of the powders are shown in Figure 1 along with the particle size percentile values in Table 2. It is seen that all of the powders have a near spherical morphology, with the CoCrFeNi showing some non-spherical satellite particles. It is also shown that the average particle size of the Cu powder is 40.0 µm which is larger than that of the CoCrFeNi and Ti powders. There has been some limited research completed into AM of powders of different particle size distributions where smaller particles were interstitial between larger particles resulting in a higher packing density and a more homogeneous part [48]. However, the particle size difference in this case is not enough for the CoCrFeNi to be interstitial in the packing of the larger Cu particles, therefore it is assumed that both powder mixes will result in comparable packing densities.

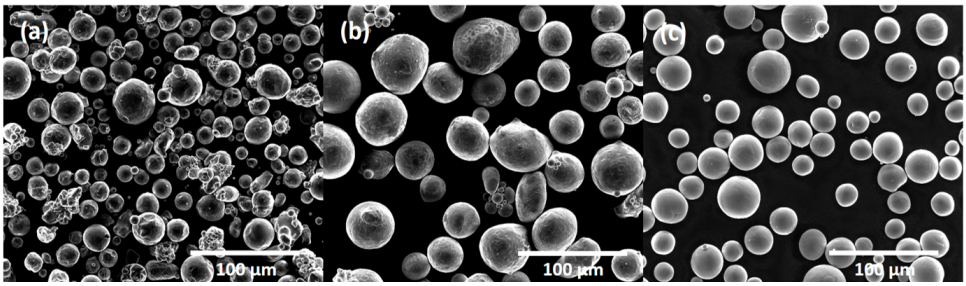

Figure 1. Secondary electron images images of the powders used for SLM. (**a**) CoCrFeNi, (**b**) Cu, (**c**) Ti.

Table 2. Particle diameter percentile values prior to mixing from the laser diffraction particle size distribution for each of the powders. Where D_{10}, D_{50} and D_{90} are the 10th, 50th and 90th percentile values of the particle diameter distribution for each powder.

Powder	D_{10} (µm)	D_{50} (µm)	D_{90} (µm)
CoCrFeNi	17.9	30.1	49.0
Cu	26.5	40.0	59.8
Ti	19.9	29.2	42.8

3.2. Processing Parameters and Density

Representative optical micrographs for the highest relative density condition for each alloy are shown in Figure 2. Table 3 shows the corresponding parameters, relative density and Volume Energy Density (VED) for each of the micrographs shown in Figure 2. VED is calculated by using the equation:

$$VED = P/vht, \quad (1)$$

where P is the laser power (W), v is the scanning velocity (mm/s), h is the hatch spacing (µm) and t is the layer thickness (µm).

From Figure 2 and Table 3, it can be seen that CoCrFeNi has an extremely high relative density. This is not unexpected, as this alloy in pre-alloyed powder form has been shown to be highly compatible with SLM in previous work [2]. The optimal input VED for this alloy (from those explored) was also considerably higher than that of the alloys with additions, resulting in some small keyholes, but notably no solidification cracking or hot tearing. The lack of such defects suggests that the solid solution microstructure seen previously is likely stable in SLM, as if there were high levels of micro-segregation, solidification cracks would have formed. The appearance of small keyholes indicates the the VED here is most likely at the higher end of the processing window for this alloy.

Figure 2 and Table 3 also show a high relative density of 99.13% was achieved for the CoCrFeNiCu alloy. The input VED necessary for this density was considerably lower than that required for the alloy without Cu. This could be due to the fact that copper has a lower melting point than the other constituent elements, as well as it being highly thermally conductive. Meaning that it could possibly be melting at a lower temperature and result in more effective heat transfer within the melt pool and in solidification. The porosity seen in this sample in image (b) in Figure 2 appears to be caused mainly by lack of fusion, where powder has not been completely melted in some areas. There also is some solidification cracking seen, which is much more prevalent the samples with higher VED. The lack of fusion indicates that the VED used for this sample is at the lower boundary of the processing window for this alloy and further work is needed to try and narrow down which parameters would result in dense parts.

Results from the CoCrFeNiTi build with highest density are also shown in Figure 2 and Table 3. This shows a vastly reduced relative density compared to the other alloys manufactured. There is extensive cracking seen in this alloy, unlike the other alloys, as well as some larger, wider pores, suggesting that the addition of Ti has increased the crack susceptibility. The VED for this sample was also very low, but as most of the porosity is likely to be caused by cracking as well as lack of fusion, relating VED to the highest relative density is not necessarily useful in this case. If the VED were increased, the level of cracking would also probably increase, but the porosity caused by lack of fusion would decrease. The cause of the cracking seen in this alloy is further explored in Section 3.4.

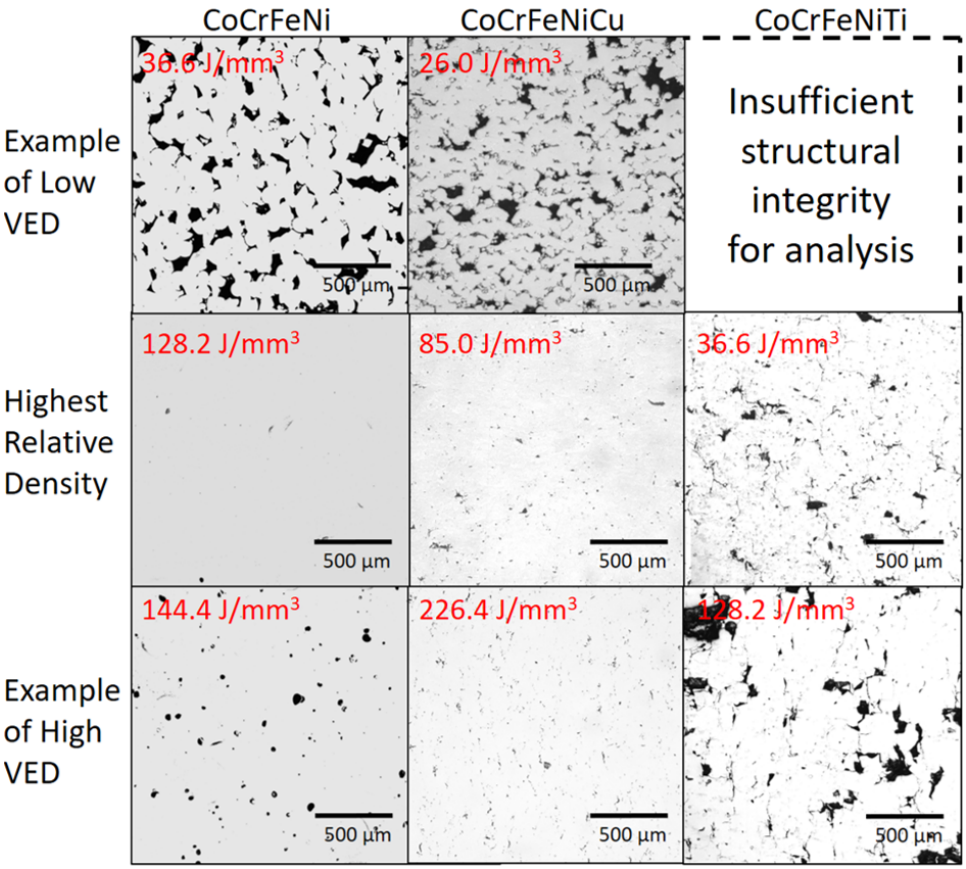

Figure 2. Optical Microscopy images of highest relative density sample, as well as examples of samples with low and high VED, for each alloy resulting from the DOE. VED values for each sample are shown in red. All scale bars are 500 µm. The low VED sample for the CoCrFeNiTi alloy had insufficient structural integrity for sectioning and subsequent analysis.

Table 3. SLM processing parameters and the calculated VED for the sample with highest relative density for each alloy.

Alloy	Relative Density (%)	Laser Power P (W)	Scanning Velocity v (mm/s)	Hatch Spacing h (µm)	Layer Thickness t (µm)	VED (J/mm^3)
CoCrFeNi	99.88	94	582	42	30	128.2
CoCrFeNiCu	99.13	130	850	60	30	85.0
CoCrFeNiTi	95.61	70	850	75	30	36.6

For each of the alloys manufactured by SLM, the relative density has been plotted against the input VED in Figure 3. CoCrFeNi shows a clear trend relating density and VED, where the highest density parts are likely to be seen where VED is between 60 J/mm^3–130 J/mm^3. At a VED lower than this range, parts have reduced density due to lack of fusion. If the VED is higher than this range, parts have reduced density due to excessive keyhole formation. A similar, but less well defined, trend can be seen for CoCrFeNiCu. It is suspected that the addition of Cu could cause localised variation in thermal properties, so porosity is perhaps more variable than in the purely pre-alloyed powder. There is a definite VED range where parts with a consistently high density are made, between 75 J/mm^3–125 J/mm^3. There is no trend seen in the plot for CoCrFeNiTi, due to the formation of cracks, via a mechanism not seen in the other alloys. At a lower VED there is lack of fusion and fewer cracks but at a higher VED there is the appearance of some keyholes but a vast increase in cracking. So, because of the higher crack susceptibility of this alloy, it is difficult to define a firm processing window in this case. This explains why the VED for the highest density sample of this alloy, shown in Table 3, is so low, as cracking is reduced. It should be noted that alternative measures such as normalised energy density could offer different insights into material process-ability, however they could not be utilised in this case, due to the unknown thermal properties of the materials [49].

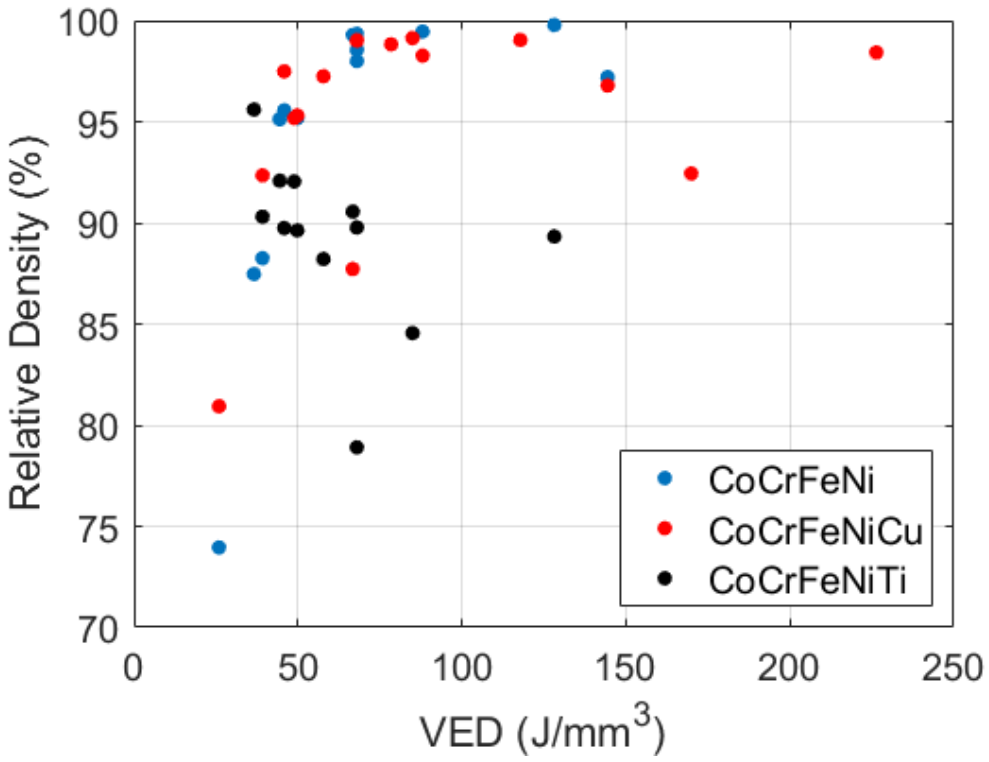

Figure 3. Plots for each alloy, showing relative densities of each part for the corresponding input VED.

3.3. XRD

XRD results given in Figure 4 show that both the CoCrFeNi and CoCrFeNiCu have a FCC microstructure with similar lattice parameters. The CoCrFeNiCu shows some peak broadening compared to the CoCrFeNi, indicative of a variation in lattice parameter. This could be caused by the uneven distribution of copper which could be causing some additional lattice distortion in some areas. The CoCrFeNiTi alloy shows an FCC phase, but also the appearance of peaks relating to the NiTi intermetallic and a Laves Hexagonal Close Packed (HCP) phase which is most likely $TiCo_2$. The FCC peaks are also quite broad, suggesting there is some variation in the lattice parameter caused by the Ti not being homogeneously distributed throughout the FCC phase, in a similar manner to Cu in the previous alloy.

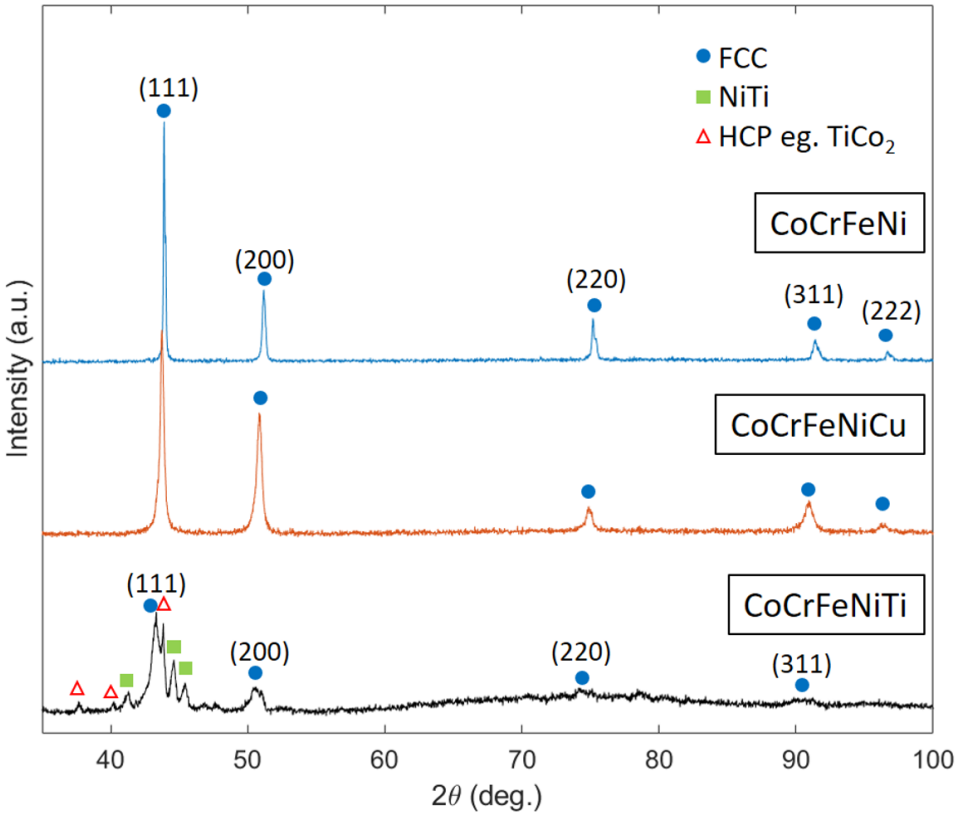

Figure 4. XRD patterns using Cu K_α radiation for CoCrFeNi, CoCrFeNiCu and CoCrFeNiTi samples. For CoCrFeNi, CoCrFeNiCu and CoCrFeNiTi the lattice parameter for the FCC phase in each case is $a \approx 3.57$ Å, $a \approx 3.58$ Å and $a \approx 3.61$ Å respectively.

3.4. Microstructure

SEM results for each alloy are shown in Figure 5. XRD showed a single phase FCC microstructure for the CoCrFeNi alloy, as seen in previous research into this composition [2]. This result is further confirmed by the EDS maps shown in Figure 5a, where elements are seen to be homogeneously distributed.

XRD analysis of the CoCrFeNiCu alloy in Figure 4 showed an apparent single phase FCC structure. It can be seen from EDS however that there is quite a substantial variation in the composition of phases within the alloy, with one phase highly enriched in Cu and the other depleted in Cu but roughly equiatomic in other elements. This is in line with the results of other work examining this alloy system produced by other manufacturing methods [46,50]. It is likely the second phase enriched in Cu has a lattice parameter near to that of pure Cu ($a \approx 3.6149$ Å). However, this phase was not easily resolved by XRD as it is evidently less abundant that the other phase and the peaks may have superimposed

with the peaks of the other more abundant phase. It is noteworthy that the peaks on the CoCrFeNiCu case appear to be broadened, which may be evidence of this effect.

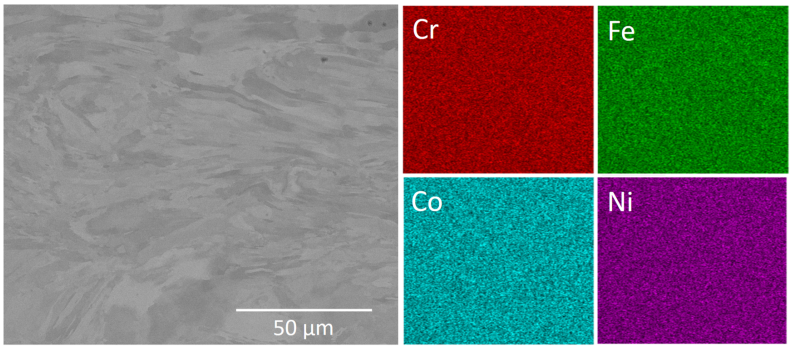

(**a**) CoCrFeNi

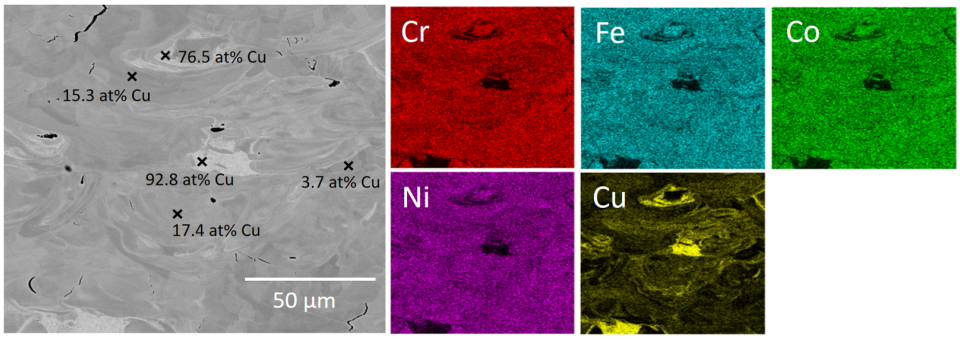

(**b**) CoCrFeNiCu

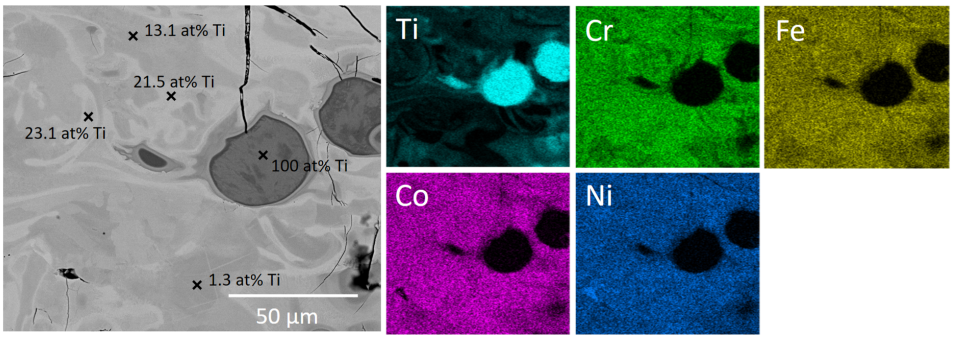

(**c**) CoCrFeNiTi

Figure 5. Back Scattered Electron (BSE) images and accompanying EDS scans of the (**a**) CoCrFeNi, (**b**) CoCrFeNiCu and (**c**) CoCrFeNiTi alloys. EDS point scans showing the variation in concentration of Cu and Ti have also been shown, where all other elements remained equiatomic.

As outlined in work by Verma et al., Cu has a positive enthalpy of mixing with all other elements in this alloy, so will not mix with them under equilibrium conditions [50]. The microstructure seen in that previous work showed Cu-rich second phase at the grain boundaries with a homogeneous distribution throughout. However in this work it is likely that the combination of elemental Cu powder with CoCrFeNi pre-alloyed powder, followed by the use of the SLM process for in-situ alloying, has exacerbated this phenomenon. The most Cu rich regions are of similar size to the elemental powder particles at 15–45 µm and EDS point scans show that these regions are between 75–92 at% Cu with other elements at equiatomic proportions. This is suggestive of the copper not properly mixing with the rest of the alloy in the molten state, and retaining some of the distribution it had as powder. The Cu depleted phase still contains between 3–17 at% Cu, showing there has been some diffusion of the Cu into the main FCC phase. Perhaps due to the high cooling rates and

rapid solidification in SLM this Cu was trapped in the FCC lattice rather than being able to segregate to the full extent on the grain boundaries as in equilibrium conditions.

EDS results for the CoCrFeNiTi alloy are shown in Figure 5c. Firstly, it is clear to see that there are un-melted Ti particles, where EDS point scans show that no alloying has taken place. This clearly demonstrates the input VED in this case did not cause a temperature high enough to melt or dissolve those particles, as discussed in Section 3.2. The un-melted particles appear to have served as crack initiation sites for some examples of the extensive cracking seen throughout this sample. These cracks generally seem to propagate through the grains and are very straight and angular, which is characteristic of solid-state cracking due to residual stress rather than the jagged edges produced by solidification cracking. A similar example of this type of solid-state cracking is seen in work by Zhang et al. on the CoCrFeNiMn alloy, where solid-state cracks initiated from smaller solidification cracks and propagated along high angle grain boundaries [51]. From EDS point scans it can be seen that the proportion of Ti varies between 1.3 at% to 23 at% in the vicinity of the un-melted Ti particles with all other elements remaining equiatomic throughout. It is clear that the intermetallic and brittle phases are distributed throughout an FCC matrix and not segregated at the grain boundaries as seen in the previous work mentioned, and this would explain why crack propagation is through grains themselves.

As seen in Section 3.2, it has not been possible to define an optimum build processing window for this alloy and this is further confirmed by microstructural analysis. For this alloy, the in-situ alloying process was not completely successful, as there were still unalloyed Ti particles present. This could be due at least partially to its higher melting point than the other elements. A higher VED would be necessary to melt or dissolve the Ti particles; however an increase in VED will only increase the severity of the residual stress cracking.

4. Discussion

In this work, SLM builds of CoCrFeNi, CoCrFeNiCu and CoCrFeNiTi were completed where the SLM process itself was used for in-situ alloying of the additional powders (Cu and Ti) to the pre-alloyed CoCrFeNi powder. A DOE was completed for each alloy and the part determined to have the highest density by image analysis for each alloy was further analysed by XRD and SEM/EDS.

The CoCrFeNi build resulted in a part with a high relative density and a homogeneous single phase FCC microstructure with a clear processing window, as seen in Figure 3. The CoCrFeNiCu alloy resulted in a high relative density and showed a wider possible processing window. The microstructure showed two FCC phases—one depleted and one enriched in Cu. The Cu particles did alloy with the pre-alloyed powder, but due to the tendency for Cu to segregate in this alloy there were large areas of high concentrations of Cu. These were much larger than the grain boundary segregation seen in this alloy manufactured by other methods [50]. The CoCrFeNiTi alloy had very low relative density and showed extensive cracking due to residual stresses. There was no distinct processing window for this alloy as increased VED resulted in increased cracking and reducing the VED resulted in unmelted Ti particles and lack of fusion defects. The microstructure was shown to have an FCC matrix with the presence of NiTi and a HCP phase, as cracks propagated through the grains not along grain boundaries.

The in-situ alloying process was more successful in the case of the Cu, as Cu particles were at least partially alloyed with the pre-alloyed elements. This is likely because the melting point of Cu at 1084 °C is much lower than that of CoCrFeNi at 1414 °C and the melting point of Ti is higher at 1688 °C. Therefore, Cu will more readily dissolve into solid solution or melt at lower temperatures than Ti. This indicates that in future alloy development using this method, consideration should go into the additional elemental powder melting point relative to the base powder. There also should be some consideration of whether the additional element commonly causes grain boundary segregation in that alloy, if that alloy has been manufactured previously by AM or by other means. If that

element tends to segregate then adding it as an addition to a pre-alloyed powder will result in highly segregated wider regions with a differing morphology to common grain boundary segregation. Also in this case, most likely due to rapid cooling, elements like Cu have been incorporated into the main phase in varying levels throughout the sample, which differs from the alloy when produced by methods with slower cooling rates. Therefore in order to compare alloys manufactured in this way to those by conventional methods, subsequent heat treatment steps would be necessary to homogenise the microstructure.

5. Conclusions

In this work, elemental Cu and Ti powders were mixed with pre-alloyed CoCrFeNi powder, in equiatomic proportions, and then alloyed in-situ via SLM. The corresponding microstructure of the sample with highest relative density for each alloy was then analysed. The main findings of this work are summarised as follows:

- The build of the CoCrFeNi alloy resulted in a sample with high relative density at a VED of 128.2 J/mm^3 and single phase FCC microstructure with a clear and wide processing window.
- The build of the CoCrFeNiCu alloy showed high relative density, a well-defined processing window and two FCC phases; one depleted and one rich in Cu. The VED which produced the highest relative density was low at 85.0 J/mm^3 compared to that of the CoCrFeNi, most likely due to the addition of Cu which has a lower melting point. The Cu did alloy with the pre-alloyed base powder but there were large areas of high Cu concentration due to its inherent tendency to segregate with the other constituent elements.
- The build of CoCrFeNiTi show a low relative density and no clear processing window. Some Ti particles remained un-melted, while some Ti had alloyed to produce brittle intermetallic NiTi and HCP phases in an FCC matrix. There was extensive solid-state residual stress cracking seen in every sample. The VED which resulted in the sample of highest density was low at 36.6 J/mm^3, as this was the sample in which the least cracking occurred even though there was some lack of fusion porosity.
- A component of the success of in-situ alloying is deemed dependent on the melting temperature of the elemental powder being less than or comparable to the melting temperature of the base alloy powder. In this case the melting temperature of Cu (1084 °C) is much lower than that of CoCrFeNi (1414 °C) and the melting point of Ti is higher (1688 °C), resulting in un-melted Ti particles.
- The tendency of the additional element to segregate at grain boundaries, in the same alloy manufactured by other methods, should also be an indicator of whether that elemental addition is suitable for in-situ alloying. If the element tends to segregate, like Cu in this study, this can result in areas of high concentration of that element, with a differing morphology to common grain boundary segregation.

Finally, It has been shown that in-situ alloying could be a useful tool with which to develop novel alloys quickly. In the future, further work involving heat treatments of in-situ alloyed samples could possibly result in a more homogeneous microstructure, therefore expanding the range of elements which could be added and alloyed successfully.

Author Contributions: Conceptualization, L.F., I.T. and R.G.; methodology, L.F., I.T. and R.G.; investigation, L.F., G.M., L.H. and F.L.; original draft preparation, L.F.; review and editing, F.L. and R.G.; supervision, I.T. and R.G. All authors have read and agreed to the published version of the manuscript.

Funding: This work was supported by Science Foundation Ireland 18/EPSRC-CDT/3584, the Engineering and Physical Sciences Research Council EP/S022635/1 and the Manufacture using Advanced Powder Processes (MAPP) EPSRC Future Manufacturing Hub EP/P006566/1. We wish to acknowledge the Henry Royce Institute for Advanced Materials, funded through EPSRC grants EP/R00661X/1, EP/S019367/1, EP/P02470X/1 and EP/P025285/1, for access to the Aconity3D Mini at The University of Sheffield.

Institutional Review Board Statement: Not applicable.

Informed Consent Statement: Not applicable.

Data Availability Statement: Data are available on request from the corresponding author, as they form part of an ongoing study.

Conflicts of Interest: The authors declare no conflict of interest.

References

1. Yeh, J.W.; Chen, S.K.; Lin, S.J.; Gan, J.Y.; Chin, T.S.; Shun, T.T.; Tsau, C.H.; Chang, S.Y. Nanostructured high-entropy alloys with multiple principal elements: Novel alloy design concepts and outcomes. *Adv. Eng. Mater.* **2004**, *6*, 299–303. [CrossRef]
2. Brif, Y.; Thomas, M.; Todd, I. The use of high-entropy alloys in additive manufacturing. *Scr. Mater.* **2015**, *99*, 93–96. [CrossRef]
3. Wu, Z.; Bei, H.; Otto, F.; Pharr, G.M.; George, E.P. Recovery, recrystallization, grain growth and phase stability of a family of FCC-structured multi-component equiatomic solid solution alloys. *Intermetallics* **2014**, *46*, 131–140. [CrossRef]
4. Salishchev, G.A.; Tikhonovsky, M.A.; Shaysultanov, D.G.; Stepanov, N.D.; Kuznetsov, A.V.; Kolodiy, I.V.; Tortika, A.S.; Senkov, O.N. Effect of Mn and v on structure and mechanical properties of high-entropy alloys based on CoCrFeNi system. *J. Alloys Compd.* **2014**, *591*, 11–21. [CrossRef]
5. Cantor, B.; Chang, I.T.; Knight, P.; Vincent, A.J. Microstructural development in equiatomic multicomponent alloys. *Mater. Sci. Eng. A* **2004**, *375–377*, 213–218. [CrossRef]
6. Ostovari Moghaddam, A.; Shaburova, N.A.; Samodurova, M.N.; Abdollahzadeh, A.; Trofimov, E.A. Additive manufacturing of high entropy alloys: A practical review. *J. Mater. Sci. Technol.* **2021**, *77*, 131–162. [CrossRef]
7. Torralba, J.M.; Campos, M. High entropy alloys manufactured by additive manufacturing. *Metals* **2020**, *10*, 639. [CrossRef]
8. Zhang, H.; Pan, Y.; He, Y.Z. Synthesis and characterization of FeCoNiCrCu high-entropy alloy coating by laser cladding. *Mater. Des.* **2011**, *32*, 1910–1915. [CrossRef]
9. Yao, J.; Weng, Z.; Dong, G.; Yang, L. Microstructure and hardness of FeCrNiCoMn high-entropy alloy coating prepared by laser cladding with pre-alloyed gas atomized powder. In Proceedings of the ICALEO 2013—32nd International Congress on Applications of Lasers and Electro-Optics, Miami, FL, USA, 8–10 October 2013; Volume 480, pp. 480–486. [CrossRef]
10. Zhang, C.; Chen, G.J.; Dai, P.Q. Evolution of the microstructure and properties of laser-clad FeCrNiCoBx high-entropy alloy coatings. *Mater. Sci. Technol.* **2016**, *32*, 1666–1672. [CrossRef]
11. Muangtong, P.; Rodchanarowan, A.; Chaysuwan, D.; Chanlek, N.; Goodall, R. The corrosion behaviour of CoCrFeNi-x (x = Cu, Al, Sn) high entropy alloy systems in chloride solution. *Corros. Sci.* **2020**, *172*, 108740. [CrossRef]
12. Qiu, Z.; Yao, C.; Feng, K.; Li, Z.; Chu, P.K. Cryogenic deformation mechanism of CrMnFeCoNi high-entropy alloy fabricated by laser additive manufacturing process. *Int. J. Lightweight Mater. Manuf.* **2018**, *1*, 33–39. [CrossRef]
13. Xiang, S.; Luan, H.; Wu, J.; Yao, K.F.; Li, J.; Liu, X.; Tian, Y.; Mao, W.; Bai, H.; Le, G.; et al. Microstructures and mechanical properties of CrMnFeCoNi high entropy alloys fabricated using laser metal deposition technique. *J. Alloys Compd.* **2019**, *773*, 387–392. [CrossRef]
14. Xiang, S.; Li, J.; Luan, H.; Amar, A.; Lu, S.; Li, K.; Zhang, L.; Liu, X.; Le, G.; Wang, X.; et al. Effects of process parameters on microstructures and tensile properties of laser melting deposited CrMnFeCoNi high entropy alloys. *Mater. Sci. Eng. A* **2019**, *743*, 412–417. [CrossRef]
15. Chen, P.; Li, S.; Zhou, Y.; Yan, M.; Attallah, M.M. Fabricating CoCrFeMnNi high entropy alloy via selective laser melting in-situ alloying. *J. Mater. Sci. Technol.* **2020**, *43*, 40–43. [CrossRef]
16. Cagirici, M.; Wang, P.; Ng, F.L.; Nai, M.L.S.; Ding, J.; Wei, J. Additive manufacturing of high-entropy alloys by thermophysical calculations and in situ alloying. *J. Mater. Sci. Technol.* **2021**, *94*, 53–66. [CrossRef]
17. Zhang, H.; Zhao, Y.; Huang, S.; Zhu, S.; Wang, F.; Li, D. Manufacturing and analysis of high-performance refractory high-entropy alloy via selective laser melting (SLM). *Materials* **2019**, *12*, 720. [CrossRef]
18. Zhang, H.; Xu, W.; Xu, Y.; Lu, Z.; Li, D. The thermal-mechanical behavior of WTaMoNb high-entropy alloy via selective laser melting (SLM): Experiment and simulation. *Int. J. Adv. Manuf. Technol.* **2018**, *96*, 461–474. [CrossRef]
19. Melia, M.A.; Whetten, S.R.; Puckett, R.; Jones, M.; Heiden, M.J.; Argibay, N.; Kustas, A.B. High-throughput additive manufacturing and characterization of refractory high entropy alloys. *Appl. Mater. Today* **2020**, *19*, 100560. [CrossRef]
20. Moorehead, M.; Bertsch, K.; Niezgoda, M.; Parkin, C.; Elbakhshwan, M.; Sridharan, K.; Zhang, C.; Thoma, D.; Couet, A. High-throughput synthesis of Mo-Nb-Ta-W high-entropy alloys via additive manufacturing. *Mater. Des.* **2020**, *187*, 108358. [CrossRef]
21. Wu, Y.; Liaw, P.K.; Zhang, Y. Preparation of bulk tizrnbmov and nbtialtav high-entropy alloys by powder sintering. *Metals* **2021**, *11*, 1748. [CrossRef]
22. Kuzminova, Y.; Firsov, D.; Dudin, A.; Sergeev, S.; Zhilyaev, A.; Dyakov, A.; Chupeeva, A.; Alekseev, A.; Martynov, D.; Akhatov, I.; et al. The effect of the parameters of the powder bed fusion process on the microstructure and mechanical properties of CrFeCoNi medium-entropy alloys. *Intermetallics* **2020**, *116*, 106651. [CrossRef]

23. Zhu, Z.G.; Nguyen, Q.B.; Ng, F.L.; An, X.H.; Liao, X.Z.; Liaw, P.K.; Nai, S.M.; Wei, J. Hierarchical microstructure and strengthening mechanisms of a CoCrFeNiMn high entropy alloy additively manufactured by selective laser melting. *Scr. Mater.* **2018**, *154*, 20–24. [CrossRef]
24. Sun, Z.; Tan, X.; Wang, C.; Descoins, M.; Mangelinck, D.; Tor, S.B.; Jägle, E.A.; Zaefferer, S.; Raabe, D. Reducing hot tearing by grain boundary segregation engineering in additive manufacturing: Example of an AlxCoCrFeNi high-entropy alloy. *Acta Mater.* **2021**, *204*, 116505. [CrossRef]
25. Wang, P.; Huang, P.; Ng, F.L.; Sin, W.J.; Lu, S.; Nai, M.L.S.; Dong, Z.L.; Wei, J. Additively manufactured CoCrFeNiMn high-entropy alloy via pre-alloyed powder. *Mater. Des.* **2019**, *168*, 107576. [CrossRef]
26. Li, R.; Niu, P.; Yuan, T.; Cao, P.; Chen, C.; Zhou, K. Selective laser melting of an equiatomic CoCrFeMnNi high-entropy alloy: Processability, non-equilibrium microstructure and mechanical property. *J. Alloys Compd.* **2018**, *746*, 125–134. [CrossRef]
27. Kim, Y.K.; Choe, J.; Lee, K.A. Selective laser melted equiatomic CoCrFeMnNi high-entropy alloy: Microstructure, anisotropic mechanical response, and multiple strengthening mechanism. *J. Alloys Compd.* **2019**, *805*, 680–691. [CrossRef]
28. Niu, P.; Li, R.; Zhu, S.; Wang, M.; Chen, C.; Yuan, T. Hot cracking, crystal orientation and compressive strength of an equimolar CoCrFeMnNi high-entropy alloy printed by selective laser melting. *Opt. Laser Technol.* **2020**, *127*, 106147. [CrossRef]
29. Xu, Z.; Zhang, H.; Li, W.; Mao, A.; Wang, L.; Song, G.; He, Y. Microstructure and nanoindentation creep behavior of CoCrFeMnNi high-entropy alloy fabricated by selective laser melting. *Addit. Manuf.* **2019**, *28*, 766–771. [CrossRef]
30. Niu, P.D.; Li, R.D.; Yuan, T.C.; Zhu, S.Y.; Chen, C.; Wang, M.B.; Huang, L. Microstructures and properties of an equimolar AlCoCrFeNi high entropy alloy printed by selective laser melting. *Intermetallics* **2019**, *104*, 24–32. [CrossRef]
31. Karlsson, D.; Marshal, A.; Johansson, F.; Schuisky, M.; Sahlberg, M.; Schneider, J.M.; Jansson, U. Elemental segregation in an AlCoCrFeNi high-entropy alloy—A comparison between selective laser melting and induction melting. *J. Alloys Compd.* **2019**, *784*, 195–203. [CrossRef]
32. Zhou, P.F.; Xiao, D.H.; Wu, Z.; Ou, X.Q. Al0.5FeCoCrNi high entropy alloy prepared by selective laser melting with gas-atomized pre-alloy powders. *Mater. Sci. Eng. A* **2019**, *739*, 86–89. [CrossRef]
33. Ocelík, V.; Janssen, N.; Smith, S.N.; De Hosson, J.T.M. Additive Manufacturing of High-Entropy Alloys by Laser Processing. *JOM* **2016**, *68*, 1810–1818. [CrossRef]
34. Luo, S.; Gao, P.; Yu, H.; Yang, J.; Wang, Z.; Zeng, X. Selective laser melting of an equiatomic AlCrCuFeNi high-entropy alloy: Processability, non-equilibrium microstructure and mechanical behavior. *J. Alloys Compd.* **2019**, *771*, 387–397. [CrossRef]
35. Wang, Y.; Li, R.; Niu, P.; Zhang, Z.; Yuan, T.; Yuan, J.; Li, K. Microstructures and properties of equimolar AlCoCrCuFeNi high-entropy alloy additively manufactured by selective laser melting. *Intermetallics* **2020**, *120*, 106746. [CrossRef]
36. Zhang, M.; Zhou, X.; Wang, D.; Zhu, W.; Li, J.; Zhao, Y.F. AlCoCuFeNi high-entropy alloy with tailored microstructure and outstanding compressive properties fabricated via selective laser melting with heat treatment. *Mater. Sci. Eng. A* **2019**, *743*, 773–784. [CrossRef]
37. Fujieda, T.; Shiratori, H.; Kuwabara, K.; Kato, T.; Yamanaka, K.; Koizumi, Y.; Chiba, A. First demonstration of promising selective electron beam melting method for utilizing high-entropy alloys as engineering materials. *Mater. Lett.* **2015**, *159*, 12–15. [CrossRef]
38. Fujieda, T.; Shiratori, H.; Kuwabara, K.; Hirota, M.; Kato, T.; Yamanaka, K.; Koizumi, Y.; Chiba, A.; Watanabe, S. CoCrFeNiTi-based high-entropy alloy with superior tensile strength and corrosion resistance achieved by a combination of additive manufacturing using selective electron beam melting and solution treatment. *Mater. Lett.* **2017**, *189*, 148–151. [CrossRef]
39. Fujieda, T.; Chen, M.; Shiratori, H.; Kuwabara, K.; Yamanaka, K.; Koizumi, Y.; Chiba, A.; Watanabe, S. Mechanical and corrosion properties of CoCrFeNiTi-based high-entropy alloy additive manufactured using selective laser melting. *Addit. Manuf.* **2019**, *25*, 412–420. [CrossRef]
40. Liu, H.; Li, X.; Liu, J.; Gao, W.; Du, X.; Hao, J. Microstructural evolution and properties of dual-layer CoCrFeMnTi0.2 high-entropy alloy coating fabricated by laser cladding. *Opt. Laser Technol.* **2021**, *134*, 106646. [CrossRef]
41. Shun, T.T.; Chang, L.Y.; Shiu, M.H. Microstructures and mechanical properties of multiprincipal component CoCrFeNiTi x alloys. *Mater. Sci. Eng. A* **2012**, *556*, 170–174. [CrossRef]
42. Park, N.; Watanabe, I.; Terada, D.; Yokoyama, Y.; Liaw, P.K.; Tsuji, N. Recrystallization Behavior of CoCrCuFeNi High-Entropy Alloy. *Metall. Mater. Trans. Phys. Metall. Mater. Sci.* **2015**, *46*, 1481–1487. [CrossRef]
43. Chen, R.; Qin, G.; Zheng, H.; Wang, L.; Su, Y.; Chiu, Y.; Ding, H.; Guo, J.; Fu, H. Composition design of high entropy alloys using the valence electron concentration to balance strength and ductility. *Acta Mater.* **2018**, *144*, 129–137. [CrossRef]
44. Tong, C.J.; Chen, Y.L.; Chen, S.K.; Yeh, J.W.; Shun, T.T.; Tsau, C.H.; Lin, S.J.; Chang, S.Y. Microstructure characterization of AlxCoCrCuFeNi high-entropy alloy system with multiprincipal elements. *Metall. Mater. Trans. Phys. Metall. Mater. Sci.* **2005**, *36*, 881–893. [CrossRef]
45. Wu, P.H.; Liu, N.; Zhou, P.J.; Peng, Z.; Du, W.D.; Wang, X.J.; Pan, Y. Microstructures and liquid phase separation in multicomponent CoCrCuFeNi high entropy alloys. *Mater. Sci. Technol.* **2016**, *32*, 576–580. [CrossRef]
46. Rogal, Ł. Semi-solid processing of the CoCrCuFeNi high entropy alloy. *Mater. Des.* **2017**, *119*, 406–416. [CrossRef]
47. Schneider, C.A.; Rasband, W.S.; Eliceiri, K.W. NIH Image to ImageJ: 25 years of image analysis. *Nat. Methods* **2012**, *9*, 671–675. [CrossRef]
48. Farzadfar, S.A.; Murtagh, M.J.; Venugopal, N. Impact of IN718 bimodal powder size distribution on the performance and productivity of laser powder bed fusion additive manufacturing process. *Powder Technol.* **2020**, *375*, 60–80. [CrossRef]

49. Thomas, M.; Baxter, G.J.; Todd, I. Normalised model-based processing diagrams for additive layer manufacture of engineering alloys. *Acta Mater.* **2016**, *108*, 26–35. [CrossRef]
50. Verma, A.; Tarate, P.; Abhyankar, A.C.; Mohape, M.R.; Gowtam, D.S.; Deshmukh, V.P.; Shanmugasundaram, T. High temperature wear in CoCrFeNiCux high entropy alloys: The role of Cu. *Scr. Mater.* **2019**, *161*, 28–31. [CrossRef]
51. Zhang, C.; Feng, K.; Kokawa, H.; Han, B.; Li, Z. Cracking mechanism and mechanical properties of selective laser melted CoCrFeMnNi high entropy alloy using different scanning strategies. *Mater. Sci. Eng. A* **2020**, *789*, 139672. [CrossRef]